Different physicochemical behaviors of nitrate and ammonium during transport: a case study on Mt. Hua, China

Can Wu[1], Cong Cao[2,a], Jianjun Li[2], Shaojun Lv[1], Jin Li[2,b], Xiaodi Liu[1], Si Zhang[1], Shijie Liu[1], Fan Zhang[1], Jingjing Meng[4], Gehui Wang[1,3]*

[1] Key Lab of Geographic Information Science of the Ministry of Education, School of Geographic Sciences, East China Normal University, Shanghai 200062, China
[2] State Key Laboratory of Loess and Quaternary Geology, Institute of Earth Environment, Chinese Academy of Sciences, Xi'an 710061, China
[3] Institute of Eco-Chongming, Chenjia Zhen, Chongming, Shanghai 202162, China
[4] School of Environment and Planning, Liaocheng University, Liaocheng 252000, China

[a] Now at The State University of New York at Stony Brook.
[b] Now at Institute for Environmental and Climate Research, Jinan University.

*Corresponding author. Gehui Wang (ghwang@geo.ecnu.edu.cn)

Abstract: To understand the chemical evolution of aerosols in the transport process, the chemistry of $PM_{2.5}$ and nitrogen isotope compositions on the mountainside of Mt. Hua (~1120 m a.s.l.) in inland China during the 2016 summertime were investigated and compared with parallel observations collected at surface sampling site (~400 m a.s.l.). $PM_{2.5}$ exhibited a high level at the mountain foot site (MF) (aver. 76.0±44.1 $\mu g/m^3$) and could be transported aloft by anabatic valley winds, leading to the gradual accumulation of daytime $PM_{2.5}$ with a noon peak at the mountainside sampling site (MS). As the predominant ion species, sulfate exhibited nearly identical mass concentrations in both sites, but its $PM_{2.5}$ mass fraction was moderately enhanced by ~4% at the MS site. The ammonium variations were similar to the sulfate variations, the chemical forms of both of which mainly existed as ammonium bisulfate (NH_4HSO_4) and ammonium sulfate (($NH_4)_2SO_4$) at the MF and MS sites, respectively. Unlike sulfate and ammonium, nitrate mainly existed as ammonium nitrate (NH_4NO_3) in fine particles and exhibited decreasing mass concentration and proportion trends with increasing elevation. This finding was ascribed to NH_4NO_3 volatilization, in which gaseous HNO_3 from semi-volatile NH_4NO_3 subsequently reacted with dust particles to form nonvolatile salts, resulting in significant nitrate shifts from fine particles into coarse particles. Such scavenging of fine-particle nitrate led to an enrichment in the daytime ^{15}N of nitrate at the MS site compared with to the MF site. In contrast to nitrate, at the MS site, the ^{15}N in ammonium depleted during the daytime. Considering the lack of any significant change in ammonia (NH_3) sources during the vertical transport process, this ^{15}N depletion in ammonium was mainly the result of unidirectional

58　reactions, indicating that additional NH_3 would partition into particulate phases and

59　further neutralize HSO_4^- to form SO_4^{2-}. This process would reduce the aerosol acidity,

60　with a higher pH (3.4±2.2) at MS site and lower ones (2.9±2.0) at MF site. Our work

61　provides more insight into physicochemical behaviors of semi-volatile nitrate and

62　ammonium, which will facilitate the improvement in model for a better simulation of

63　aerosol composition and properties.

64　**Keywords:** Ammonium; Nitrate; Stable nitrogen isotope; Haze; Volatilization

65

66

67

68

69

70

71

72

73

74

75

76

77

78

79

1 Introduction

Atmospheric particulate matter measuring equal to or less than 2.5 μm in aerodynamic diameter (PM$_{2.5}$) is a worldwide air pollution burden that can deteriorate the urban air quality and induce adverse human health effects that contribute to lowering life expectancies (Shiraiwa et al., 2017; Lelieveld et al., 2015; Fuzzi et al., 2015; Wang et al., 2016). Recent studies have disclosed that the mechanisms underlying these effects are profoundly dependent on particle properties, e.g., the size, concentration, mixing state and chemical compositions of particles (Li et al., 2016; Liu et al., 2021; Guo et al., 2014). Thus, since 2013, China has issued strict emission directives to mitigate haze pollution. Consequently, the annual PM$_{2.5}$ concentration in China fell by approximately one-third from 2013–2017 (Zheng et al., 2018). Notwithstanding, the PM$_{2.5}$ levels in most cities in China still exceed the least-stringent target of the World Health Organization (WHO 2021; 35 μg/m^3), especially in rural areas and small cities (Lv et al., 2022; Li et al., 2023).

Near-surface PM can also be transported to the upper air, and this process critically impacts radiative forcing, cloud precipitation and the regional climate by scattering/absorbing solar radiation and by influencing aerosol-could interactions (Van Donkelaar et al., 2016; Andreae and Ramanathan, 2013; Fan et al., 2018). Past assessments of these effects have been characterized by large uncertainties (Carslaw et al., 2013); for example, Bond et al. (2013) found that black carbon climate forcing varied from +0.17 W/m^2 to +2.1 W/m^2 with a 90% uncertainty. Such massive uncertainties are mainly due to our limited knowledge regarding the spatiotemporal

102 distribution, abundance and compositions of airborne PM (Seinfeld and Johnh, 2016;

103 Raes et al., 2000). In addition, aerosols may undergo aging during the vertical transport

104 process, causing increasingly complex compositions and changes in aerosol properties.

105 Despite these factors, to date, vertical observations remain comparatively scarce

106 compared to surface measurements. Therefore, to obtain an improved understanding of

107 the fundamental chemical and dynamical processes governing haze development, more

108 field observations of upper-layer aerosols are necessary, as these measurements could

109 provide updated kinetic and mechanistic parameters that could serve to improve model

110 simulations.

111   Currently, various monitoring approaches have been developed and applied to

112 measure vertical aerosols, e.g., satellite remote sensing and in situ lidar methods; these

113 approaches can be used to obtain the pollution concentration profiles (Van Donkelaar

114 et al., 2016; Reid et al., 2017). To accurately measure chemical compositions, aircraft

115 and unmanned aerial vehicles (UAVs) equipped with a variety of instruments can be

116 utilized in short-term sampling campaigns (Lambey and Prasad, 2021; Zhang et al.,

117 2017), but these tools are unsuitable for long-term continued observations due to their

118 high operational costs. In cases of near-surface vertical urban atmosphere observations,

119 techniques involving tethered balloons, meteorological towers and skyscrapers are

120 usually adopted (Zhou et al., 2020; Xu et al., 2018; Fan et al., 2021). However, the

121 vertical application range of these methods are limited to only ~500 m, thus hardly

122 meeting the requirements of research conducted above the boundary layer. Therefore,

123 high-elevation mountain sites have long been regarded as suitable places for long-term

research on the upper-layer aerosol (including its compositions, chemical-physical

properties and formation processes, etc.) (Dzepina et al., 2015; Zhou et al., 2021; Wang

et al., 2013), which are conducive to better understanding of the haze episodes in the

lower troposphere. Although the fixed observation position is the key drawback of this

monitoring approach, it has still been widely selected for use in various vertical

observation campaigns, e.g., in past studies conducted in Salt Lake Valley (Baasandorj

et al., 2017), in Terni Valley (Ferrero et al., 2012) and on Mt. Tai (Meng et al., 2018;

Wang et al., 2011).

Mt. Hua adjoins the Guanzhong Basin of inland China, where haze pollution has

been a persistent environmental problem (Wu et al., 2020b; Wu et al., 2021; Wang et

al., 2016). In our previous studies conducted at the mountaintop of Mt. Hua, we found

that air quality was significantly affected by surface pollution, and distinctive

differences were found in the aerosol compositions and size distributions at the

mountaintop compared to those measured at lower elevations ground level (Wang et al.,

2013; Li et al., 2013). With the implementation of strict emission controls, the

atmospheric environment in this region has changed dramatically from the SO_2/sulfate-

dominated previous environment to the current NOx/nitrate-dominated environment

(Baasandorj et al., 2017; Wu et al., 2020c). However, the fundamental chemical and

dynamical processes driving this $PM_{2.5}$-loading explosion are unclear under the current

atmospheric state with increasing O_3 and NH_3 levels. To better rationalize these

processes, in this work, 4-hr integrated aerosol samples were synchronously collected

on the mountainside and at the lower-elevation land surface, and the chemical

components and stable nitrogen isotope compositions of nitrate and ammonium were analyzed in the collected $PM_{2.5}$ samples. We compared the chemical compositions and diurnal cycles between the two sampling sites and then discussed the changes in the chemical forms of secondary inorganic ions during their vertical transport from lower to higher elevations. Our study revealed that nitrate and ammonium exhibited distinct physicochemical behaviors during the aerosol-aging process.

2 Experiment

2.1 Sample collection

In this campaign, the $PM_{2.5}$ samples were synchronously collected at two locations in the Mt. Hua area during the period from 27 August to 17 September 2016. One sampling site was located on a building belonging to the Huashan Meteorological Bureau (34°32′N, 110°5′E, 400 m a.s.l.) at the foot of Mt. Hua. Surrounded by several traffic arteries and dense residential and commercial buildings, as shown in Figure 1b, this site is an ideal urban station for studying the impacts of anthropogenic activities on local air quality and is referred to hereafter as the "MF" site. The mountainous sampling site (34°29′N, 110°3′E, 1120 m a.s.l.) was located approximately 8 km from the city site horizontally (Figure 1c) at an elevation of 720 m above the average Huashan town level of ~400 m (a.s.l.). This site was situated on a mountainside that experiences little anthropogenic activity due to its steep terrain and is abbreviated hereafter as the "MS" site. Furthermore, this location adjoins one of the larger valleys of Mt. Hua; therefore, the measurements taken at this location were strongly affected by the lower-elevation air pollutants transported upwards by the valley winds. At both measurement sites, the

7

PM$_{2.5}$ aerosol samples with a 4-hr interval in were collected onto prebaked (at 450°C

for 6 hrs) quartz filters using high-volume (1.13-m^3/min) air samplers (Tisch

Environmental, Inc., USA). All air samplers were installed on the roofs of buildings,

approximately 15 m above the local ground surface. Furthermore, size-resolved aerosol

sampling was synchronously conducted at two sites during summertime (10-22 August,

2020); and these samples with nine size bins (cutoff points were 0.43, 0.65, 1.1, 2.1,

3.3, 4.7, 5.8 and 9.0 μm, respectively) were collected using an Anderson sampler at an

airflow rate of 28.3 L/min for ~72 h. After sampling, the filter samples were stored in a

freezer (at -18°C) prior to analysis.

The hourly PM$_{2.5}$, NOx and O$_3$ mass concentrations were detected at the

mountainside sampling site using an E-BAM, a chemiluminescence analyzer (Thermo,

Model 42i, USA) and a UV photometric analyzer (Thermo, Model 49i, USA),

respectively. At the MF site, only PM$_{2.5}$ was monitored, using another E-BAM, while

the data of the other species were downloaded from the Weinan Ecological

Environment Bureau (http://sthjj.weinan.gov.cn/ (last access: 8 July 2021)).

Meteorological data characterizing both sampling sites throughout the whole campaign

were obtained from the Shaanxi Meteorological Bureau website (http://sn.cma.gov.cn/

(last access: 8 July 2021)).

2.2 Chemical analysis

Four punches (1.5-cm diameter) of each aerosol sample were extracted into 10-mL

Milli-Q pure water (18.2 MΩ) under sonication for 30 min. Subsequently, the extracts

were filtered with 0.45-μm syringe filters and detected for water-soluble ions (Na$^+$,

8

190 NH_4^+, K^+, Mg^{2+}, Ca^{2+}, SO_4^{2-}, NO_2^-, NO_3^- and Cl^-) by using ion chromatography; the

191 detection limit for these nine ions was < 0.01 μg/mL. A DRI-model 2001 thermal–

192 optical carbon analyzer was used herein following the IMPROVE-A protocol to analyze

193 the organic carbon (OC) and elemental carbon (EC) in each $PM_{2.5}$ filter sample (in

194 0.526 cm^2 punches). For more details regarding the utilized methods, readers can refer

195 to our previous studies (Wu et al., 2020b).

196 To quantify the stable nitrogen isotope compositions of nitrate ($\delta^{15}N$-NO_3^-) and

197 ammonium ($\delta^{15}N$-NH_4^+) in $PM_{2.5}$ samples, the filter samples were pretreated as

198 described for the water-soluble ion analysis. The ammonium in the extracts

199 (approximately half of the resulting solution) was oxidized by hypobromite (BrO^-) to

200 nitrite (NO_2^-), which was subsequently reduced by hydroxylamine (NH_2OH) in a

201 strongly acidic environment. The above product (N_2O) was then analyzed by a

202 commercially available purge and cryogenic trap system coupled to an isotope ratio

203 mass spectrometer (PT-IRMS). A bacterial method (*Pseudomonas aureofaciens*, a

204 denitrifying bacterium without N_2O reductase activity) was used herein to convert the

205 sample NO_3^- into N_2O, which was ultimately quantified through PT-IRMS. As revealed

206 in previous studies (Fang et al., 2011), the presence of NO_2^- in aerosols may interfere

207 with the denitrifier method when measuring $\delta^{15}N$. Nonetheless, NO_2^- generally

208 composed tiny portions in most of our samples and, on average, contributed <1.0% to

209 NO_3^-+NO_2^-. Thus, we believed that the proportion of NO_2^- in the sample was too small

210 to affect the resulting $\delta^{15}N$ measurements based on the discussions reported by Wankel

211 et al. (2010). More details regarding the analytical artifact and quality control protocols

212 can be found elsewhere (Wu et al., 2021; Liu et al., 2014).

2.3 Concentration-weighted trajectory (CWT) analysis

214 CWT is a powerful tool used herein to reveal the potential spatial sources responsible

215 for the high $PM_{2.5}$ loadings measured on Mt. Hua; this method has been used previously

216 in similar studies (Wu et al., 2020c; Wu et al., 2020a). In this study, the CWT analysis

217 was conducted using the Igor-based tool coupled with hourly $PM_{2.5}$ concentrations and

218 12-hr air mass backward trajectories that were simulated by using the Hybrid-Single

219 Particle Lagrangian Integrated Trajectory (HYSPLIT) model (Petit et al., 2017).

2.4 Theoretical calculations of the partial pressures of NH_3 and HNO_3 and the

221 **dissociation constant of NH_4NO_3**

222 To obtain the product of the partial pressures of NH_3 and HNO_3, the NH_4NO_3

223 deliquescence relative humidity (DRH) was first calculated using equation (1) (Eq. 1).

224 The average DRH of NH_4NO_3 between the two sites was 65.0±2.9%, slightly lower

225 than the atmospheric RH (66.0±19.3%). As the works by Wexler and Seinfeld (1991)

226 and Tang and Munkelwitz (1993) revealed, aerosols are multicomponent mixtures, and

227 which the aerosol DRH is always lower than the DRH of the individual salts in the

228 particles. Thus, the actual DRH of the aerosols observed in this study would be lower

229 than the calculated DRH of NH_4NO_3. Based on these analyses, the particles would be

230 deliquescent most of the time, but for simplification, we always assumed that NH_4NO_3

231 was in an aqueous state, corresponding to the following dissociation reaction (R1):

$$\ln(\text{DRH}) = \frac{723.7}{T} + 1.6954 \qquad \text{(Eq. 1)}$$

$$NH_3(g)+HNO_3(g)\leftrightarrows NH_4^++NO_3^- \qquad\qquad\text{(R1)}$$
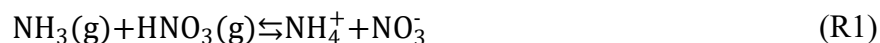
According to the approach illustrated in the referenced work (Seinfeld and Johnh, 2016), the equilibrium constant of the dissociation reaction can be described as the equation (2).

$$K_{AN}=\frac{\gamma_{NH_4NO_3}^2 m_{NH_4^+} m_{NO_3^-}}{p_{HNO_3} p_{NH_3}} \qquad\qquad\text{(Eq. 2)}$$

$$K_{AN}=4\times10^{17}\exp\left\{64.7\left(\frac{298}{T}-1\right)+11.51\left[1+\ln\left(\frac{298}{T}\right)-\frac{298}{T}\right]\right\} \qquad\text{(Eq. 3)}$$

$$\ln(K_p)=118.7-\frac{24084}{T}-6.025\ln(T) \qquad\qquad\text{(Eq. 4)}$$

where K_{AN} ($mol^2/(kg^2 \ atm^2)$) is the equilibrium constant of R1 (this value is temperature-dependent and can be calculated by Eq. 3), γ_{NH4NO3} is the binary activity coefficient for NH_4NO_3 ($\gamma_{NH4NO3}=\gamma_{NH4}\gamma_{NO3}$), and m_{NH4+} and m_{NO3-} are the molalities of NH_4^+ and NO_3^-, respectively. To calculate γ_{NH4NO3} and $m_{NH4+}m_{NO3-}$, the activity coefficients of the corresponding ions and the aerosol water content were assessed using the E-AIM (IV) model (http://www.aim.env.uea.ac.uk/aim/model4/model4a.php, (last access: 2 November 2021)). Combining equations (2) and (3), we obtained the product of the partial pressures of NH_3 and HNO_3 ($P_{HNO3}P_{NH3}$), obtaining an average of ~15.2±26.0 ppb^2 at the MF site. This value was within the range of values (1.0~37.7 ppb^2) measured by the IGAC in the summer of 2017 in Xi'an, a metropolitan city located in the Guanzhong Basin of inland China that has suffered from serious haze pollution (Wu et al., 2020a). Thus, we believe that $P_{HNO3}P_{NH3}$ variations can be assessed using the above method to a certain extent. For simplification, the dissociation constant of dry NH_4NO_3 particle (Kp, ppb^2) was thus applied in this study, which can be calculated as a function of temperature using Eq. 4, as was revealed by Mozurkewich

250 (1993). Despite without considering the aerosol properties (e.g, acidity, mixing state)

251 that may induce the shift of NH_4NO_3 equilibrium states, this assessment method was

252 also applied in the similar work conducted by Lindaas et al. (2021).

3 Results and discussion

3.1 Overview of PM$_{2.5}$ at both sites

3.1.1 Meteorological conditions and temporal variations in PM$_{2.5}$ concentrations

256 The temporal variations in the 4-hr PM$_{2.5}$ mass concentrations, water-soluble ions

257 and meteorological factors measured at the two sampling sites are illustrated in Figure

258 2, and the comparisons of the above variables are summarized in Table 1. The average

259 temperature (T) and relative humidity (RH) at the MF site were 23.2±4.2 °C and

260 68.9±18.2% (Table 1), respectively, and these values were characterized by marked

261 diurnal variations, as shown in Figure 2a. However, relatively cold and moist weather

262 frequently occurred at the MS site, which exhibited less pronounced diurnal T and RH

263 variations, with variations approximately 8 °C and 6% lower than the mean values

264 derived at the MF site, respectively. Windy weather (wind speed: 3.2±2.0 m/s) also

265 prevailed at this sampling site with gusts above 10.0 m/s; this condition is conducive

266 to the dissipation of pollutants.

267 Overall, the PM$_{2.5}$ concentrations measured at the MF site varied from 22.8 μg/m^3 to

268 245.6 μg/m^3, with a mean value of 76.0±44.1 μg/m^3, approximately corresponding to

269 Grade II (75 μg/m^3) of the National Ambient Air Quality Standard in China. Even so,

270 the PM$_{2.5}$ levels at Huashan town (i.e., at the MF site) were still higher than those

271 measured in many typical megacities in the summertime, e.g., Xi'an (37 μg/m^3 in

272   2017) (Wu et al., 2020b) and Beijing (46.3 $\mu g/m^3$ in 2016) (Lv et al., 2019).

273   Noticeably, stagnant meteorological conditions with increasing RH (> 77%) and

274   relatively low wind speeds (< 2.0 m/s) occurred during the relatively late stage of

275   observation, leading to a buildup of high $PM_{2.5}$ loadings (78.7 $\mu g/m^3$ to 245.6 $\mu g/m^3$).

276   Such typical haze events last approximately 4 days (12 September to 16 September,

277   2016), indicating that aerosol pollution is still severe in rural towns despite the notable

278   air quality improvements recorded in most Chinese urban areas. A similar temporal

279    $PM_{2.5}$ pattern was seen at the MS site, where the average $PM_{2.5}$ concentration

280   (47.0±38.0 $\mu g/m^3$) was only 0.62-fold that at the MF site and was within the range of

281   that measured at the summit of Mt. Tai (37.9 $\mu g/m^3$ in 2016) (Yi et al., 2021) and on

282   Mt. Lushan (55.9 $\mu g/m^3$ in 2011) (Li et al., 2015) in summertime. As shown in Figure

283   2d, a multiday episode (mean $PM_{2.5}$: 106.3 $\mu g/m^3$) also appeared at the MS site during

284   the period from 12 September to 15 September, corresponding to the days on which

285   high surface pollution was recorded. This was indicative of the potential impacts of

286   surface pollution on air quality in mountainous areas.

287   **3.1.2 Diurnal variation in $PM_{2.5}$**

288   As shown in Figure 2c and 2d, regular diurnal $PM_{2.5}$ variations were seen throughout

289   the whole campaign, especially at the MS site. To reveal the differences in the daily

290   changes in $PM_{2.5}$ between the two sampling sites, the mean diurnal cycles of hourly

291    $PM_{2.5}$ and the boundary layer height (BLH) are depicted in Figure 3. At the MF site, the

292    $PM_{2.5}$ concentration was moderately enhanced during the nighttime, with a daily

293   maximum (88.2±53.0 $\mu g/m^3$) observed at 6:00 local standard time (LST). After sunrise,

PM$_{2.5}$ exhibited a decreasing trend until ~15:00 LST, corresponding to thermally driven boundary-layer growth. Conversely, the aerosol concentrations at the MS site immediately increased as the boundary layer uplifted in the early morning and peaked at 14:00 LST, when the MS site was located completely within the interior of the boundary layer. Proverbially, anabatic valley winds prevail in mountainous regions during the daytime. Thus, the aerosol-rich air at MF site may be transported aloft by the prevailing valley breeze, leading to significantly enhanced PM$_{2.5}$ levels at the MS site in short time periods. This finding was further verified by the similar diurnal NO$_2$ pattern identified at the MS site, as illustrated in Figure S1. In the forenoon period, continuous enhancement in the NO$_2$ level was observed at the MS site, with a daily maximum of 14.4$\pm$53.0 μg/m^3 (at 11:00 LST); this maximum was ~7-fold the early-morning NO$_2$ concentration. However, O$_3$ exhibited indistinctive variations during this period, and this was indicative of less NO$_2$ being generated from photochemical reactions. As mentioned above, there are no obvious anthropogenic emission sources around the MS site; therefore, our observations indicate the remarkable transport of pollutants from the lower ground surface to higher elevations during the daytime.

Moreover, the PM$_{2.5}$ concentrations at the MS site exhibited less nighttime variation, with a modest abatement (Figure 3b). The nocturnal BLH usually remained below the elevation of the MS site; thus, the surface PM$_{2.5}$ may have contributed less to the aerosol levels at the MS site at night. To identify the potential spatial sources of nocturnal PM$_{2.5}$ at the MS site, a high-elevation CWT analysis was conducted. As illustrated in Figure 4, the CWT values in the daylight hours were mostly concentrated over the sampling

14

316 site, consistent with our above discussions. However, relatively high nighttime CWT

317 loadings were distributed on Mt. Hua and in its surrounding regions, indicating that

318 regional transport may be a major source of $PM_{2.5}$ at the MS site at night. Thus, the

319 constituents and variations in nocturnal $PM_{2.5}$ at the MS site may be mainly the results

320 of regional features. For verifying the feasibility of vertical transport of air parcel, the

321 WRF-Chem model was applied here to simulate wind filed and the divergence that

322 represents the expansion-rate of the air mass in unit time. From Figure 5(a), the

323 southerly winds prevailed at mountain foot area during the whole campaign, which

324 would blow the pollutants into the valley. And these pollutants at low-elevation can be

325 transported to the upper layer by the updrafts as indicated by the positive values of

326 vertical divergence at MF area that decreased with enhanced elevation (Figure 5(b)).

327 Besides that, we also analyzed the organic compounds in $PM_{2.5}$ samples, e.g.,

328 levoglucosan, BkF and IP+BghiP, which are major tracers for the emissions from

329 biomass burning, coal combustion and vehicle exhausts, respectively (Wang et al., 2009;

330 Wu et al., 2020b; Wang et al., 2007). From Figure S2, the indistinctive divergences of

331 diagnostic ratios and proportion of these organic tracers were found among both

332 sampling sites, suggesting an insignificant change of the corresponding emission

333 sources during the transport.

334 **3.2 Characterization of water-soluble ions in $PM_{2.5}$**

335 **3.2.1 Comparisons of water-soluble ions between the two sites**

336   Figure 6 shows the fractional contributions of the chemical compositions to the

337 $PM_{2.5}$ at both sampling sites. As summarized in Table 1, the water-soluble ion level

(WSI, 24.0±15.0 μg/m^3) at MF site was comparable to that of organic matter (OM,

OM=1.6×OC) (Wang et al., 2016), with a fractional contribution of ~31% to PM$_{2.5}$

(Figure 6). At the MS site, the WSI exhibited lower values (19.5±16.0 μg/m^3), yet the

proportion was moderately enhanced by ~6%. Notably, this elevated contribution of

WSIs was mostly attributed to sulfate and ammonium. Similar patterns in which the

secondary inorganic ions (sulfate, nitrate and ammonium, (SNA)) mass fraction

increased with altitude within the mixing height have also been observed in Terni

Valley (central Italy) (Ferrero et al., 2012) and Salt Lake Valley (US) (Baasandorj et

al., 2017). Among the SNA components, sulfate was the predominant species,

exhibiting slight mass concentration differences between the two sampling sites

(10.1±6.4 μg/m^3 versus 9.0±7.1 μg/m^3). However, an ~4% enhancement in the mass

fraction of sulfate was measured at the MS site. Ammonium also exhibited a similar

feature, accounting for ~5%-7.5% of the PM$_{2.5}$. These sulfate and ammonium mass

concentration homogeneities across the two sites were indicative of the further

formation of these two ions during transport. Unlike sulfate and ammonium, nitrate

and its proportions showed opposite trends, decreasing with elevation; this was

consistent with most of the measured components. Above variation features of SNA

among two sites were found at most of moments in the campaign, except for 12-13

September with a higher SNA concentration at MS site (Figure 2e and 2f). On these

two days MS site remained outside the boundary layers (a.s.l., ~550 m), suggesting

less effect of the surface pollutants on the aerosol upper layers. While, the precursor

masses (~12.3 μg/m^3 for SO$_2$ and 8.4 μg/m^3 for NO$_2$) were insufficient to form so

much SNA at MS site. Thus, the higher SNA aloft on above two days may be mostly

driven by regional or long-range transport. This can be verified by the CWT analysis,

of which high loadings were mainly distributed in the west and southwest areas of Mt.

Hua (Figure S3a), and the cities on the air mass transport pathways (e.g., Xi'an and

Weinan) also suffered from moderate haze pollution on these two days (Figure S3b).

On account of the different sources of $PM_{2.5}$ between these two days and the

remaining periods, the samples during 12-13 September were excluded in the

followed discussion. Whereas, the residual SNA data still exhibited the similar

variations as mentioned above, and the divergence in nitrate mass concentration and

fractional contribution to $PM_{2.5}$ among two sites even became more pronounced

(Figure S4). Moreover, distinct nitrate size distributions were also observed between

the different sites in the summertime of 2020 (Figure S5). From the Figure S5, we can

note that the nitrate at low-elevation was enriched in the fine mode with a minor peak

in the coarse fraction. However, the high-elevation nitrate exhibited a bimodal pattern

with two equivalent peaks in the fine and coarse fractions and was well correlated

with coarse mode calcium but poorly correlated with ammonium (R^2=0.51, p<0.05).

To our knowledge, ammonium nitrate, a major form of fine-mode particulate nitrate,

can be easily volatilized and converted into gas-phase NH_3 and HNO_3 (Pakkanen,

1996; Harrison and Pio, 1983). Thus, the gaseous HNO_3 volatilized from fine PM

may react with coarse-modal cations (e.g., Ca^{2+}, Mg^{2+} and Na^+) to form nonvolatile

salts, leading to that significant nitrate shifts from fine particles to large particles. A

similar phenomenon was also found in our previous study conducted at the summit of

382   Mt. Hua (Wang et al., 2013). Nonvolatile sulfate was predominantly found in the fine

383   fraction at both sampling sites, which may support this concept. More evidence for

384   this hypothesis is presented below in section 3.3.

385   The diurnal cycles of the 4-hr sulfate, nitrate and ammonium are illustrated in

386   Figure S6. As shown in Figure S6, the total SNA concentration at the MF site

387   exhibited a morning peak from 8:00-12:00 LST; this variation was quite different

388   from that of $PM_{2.5}$. Such a difference between the total SNA and $PM_{2.5}$ at the MF site

389   could partially be attributed to the lower sampling resolution and enhanced formation

390   of SNA in the morning. The diurnal total SNA pattern identified at the MS site

391   coincided with the $PM_{2.5}$ pattern, exhibiting a daily maximum reaching ~21.2±19.9

392      $\mu g/m^3$ (from 12:00-16:00 LST), a 1.2-fold increase compared to that measured at the

393   MF site. Among the SNA components, morning peaks of nitrate and ammonium (from

394   8:00-12:00 LST) were also observed at the MF site. These nitrate and ammonium at

395   MF site can contribute to that at the MS site through vertical transport, leading to a

396   significant enhancement in nitrate and ammonium concentrations aloft with the

397   afternoon peaks during 12:00-16:00 LST. Even so, the maximum nitrate concentration

398   at the MS site (6.5±7.4 $\mu g/m^3$) was still lower than that measured at the MF site

399   (8.9±6.8 $\mu g/m^3$) due to the NH_4NO_3 volatilization under the transport process, while

400   ammonium exhibited the opposite trend. This finding was consistent with the above

401   discussion. Unlike nitrate and ammonium, similar diurnal variations in sulfate were

402   observed between the two sampling sites, with daily maxima observed from 12:00-

403   16:00 at both sites. The major sulfate formation pathway during the daytime in

404　summer is the photooxidation of SO_2 with an OH radical, and the formation rate

405　facilitated by this process is much lower than that of the nitrate formation process

406　(Seinfeld and Johnh, 2016; Rodhe et al., 1981). Thus, sulfate formation may occur

407　continuously during vertical transport, leading to smaller difference in the diurnal

408　cycle of sulfate between the two sites.

409　**3.2.2 Chemical forms of SNA at both sites**

410　　As shown in Figure 6, the water-soluble ions considered herein mainly included

411　sulfate, nitrate and ammonium, which usually exist in the form of ammonium salts

412　(NH_4HSO_4, $(NH_4)_2SO_4$, NH_4NO_3, and so on). In the H_2SO_4-HNO_3-NH_3

413　thermodynamic system, H_2SO_4 and HNO_3 are neutralized by NH_3 under ammonia-

414　rich conditions and mainly exist as $(NH_4)_2SO_4$ and NH_4NO_3 in aerosols. Conversely,

415　H_2SO_4 is converted to HSO_4^- in environments with relatively low NH_3 availabilities.

416　Thus, NH_4HSO_4 and NH_4NO_3 may be the dominant aerosol components under such

417　environmental conditions (Rodhe et al., 1981; Seinfeld and Johnh, 2016). To reveal

418　the major SNA forms at the different sampling sites considered herein, the theoretical

419　ammonium concentration was calculated according to thermodynamic equilibrium

420　with the atmospheric sulfate and nitrate levels. The theoretical ammonium levels were

421　calculated as follows:

$$NH_{4\,\text{theory}}^+ = \left(\frac{[SO_4^{2-}]}{48} + \frac{[NO_3^-]}{62}\right) \times 18 \qquad \text{(Eq. 5)}$$

$$NH_{4\,\text{theory}}^+ = \left(\frac{[SO_4^{2-}]}{96} + \frac{[NO_3^-]}{62}\right) \times 18 \qquad \text{(Eq. 6)}$$

422　　where $[SO_4^{2-}]$ and $[NO_3^-]$ represent atmospheric concentrations ($\mu g/m^3$). When

423　$(NH_4)_2SO_4$ and NH_4NO_3 are the dominant species, the $NH_4^+{}_{\text{theory}}$ can be calculated

424   using equation (5). In contrast, equation (6) suggests that NH_4HSO_4 and NH_4NO_3 are

425   abundantly present in the analyzed aerosols. Figure 7 compares the measured NH_4^+

426   concentrations with the theoretical NH_4^+ concentrations derived by the two equations

427   above. As illustrated in Figure 7(a), the slope of the observational NH_4^+ values against

428   the theoretical NH_4^+ values calculated using equation (6) was much closer to unit at the

429   MF site than at the MS site, meaning that NH_4HSO_4 and NH_4NO_3 were the major

430   chemical forms of SNA at the MF site. However, the opposite pattern was revealed at

431   the MS site; thus, the upper aerosols were characterized by abundant $(NH_4)_2SO_4$ and

432   NH_4NO_3. We also found that the diurnal variations of the SNA chemical forms in $PM_{2.5}$,

433   which we mainly concerned in this study, were insignificant at both sampling sites.

434   Based on observational data collected during the 2020 summertime, the NH_3 level at

435   MF site (36.0±68.0 ppb) was ~9-fold that at MS site (4.1±2.5 ppb). Under such

436   abundant NH_3 environment, the S(VI) was in the major form of NH_4HSO_4 but

437    $(NH_4)_2SO_4$ in relatively low NH_3 environment, which was somewhat unexpected. As

438   can be inferred from earlier studies (Seinfeld and Johnh, 2016; Shi et al., 1999), the

439   NH_3 Henry's law coefficients generally increase in value as the temperature decreases.

440   Therefore, the lower temperatures measured at the MS site would create a more

441   favorable environment for ammonia, thus shifting its partitioning toward the particulate

442   phase. The HSO_4^- transported from the MF site would thus be further neutralized to

443   SO_4^{2-} by this additional ammonium during transport, leading to the significant

444   difference observed in the chemical forms of SNA between the two sites. Moreover, as

445   the chemical component change from NH_4HSO_4 to $(NH_4)_2SO_4$, the aerosol acidity

446   moderately decreased, showing a higher bulk $PM_{2.5}$ pH (3.4 ± 2.2) at relatively clean

447   upper layer and a lower value (2.9 ± 2.0) at heavily polluted grounds (Table 1). However,

448   the previous studies were generally recognized that the aerosol would become more

449   acidic when the air parcels were transported from the polluted to cleaner/remote regions

450   (Liu et al., 1996; Nault et al., 2021). As shown in Table 1, the change in aerosol liquid

451   water content (ALWC) has an indistinctive difference among both sampling sites (*t*-test,

452   p>0.05). Thus, we think that such a reduced aerosol acidity with increasing elevation

453   in our study was mainly due to the change in chemical component, which was caused

454   by the different physicochemical behaviors of the semi-volatile species nitrate and

455   ammonium during transport. More discussions are included in the following section.

456   **3.3 Physicochemical behaviors of nitrate and ammonium during transport**

457   According to the above discussion, a conceptual model illustrating the

458   physicochemical behaviors of nitrate and ammonium during vertical transport was

459   proposed to explain the chemical composition differences between the two sites. As

460   shown in Figure 8, surface air parcels containing abundant NH_4HSO_4 and NH_4NO_3

461   particles can be transported to the upper atmosphere by the prevailing valley winds,

462   and during this process, the volatile NH_4NO_3 is easily converted to gaseous NH_3 and

463   HNO_3. Subsequently, heterogeneous reactions of the gaseous HNO_3 with fugitive dust

464   occur, thus forming nonvolatile salts and resulting in the accumulation of nitrate on

465   the coarse-mode particles. However, as the temperature decreased, the NH_3 that

466   volatilized from the fine particles or was derived from the surface can re-enter the

467   particulate phase through the gas–particle partition. Therefore, $(NH_4)_2SO_4$ would be

468 formed in the aerosol phase and would gradually replace NH_4HSO_4.

469   To investigate the likelihood of NH_4NO_3 volatilization during the transport process,

470 the dissociation constant of NH_4NO_3 (Kp) and the partial pressures of gas-phase NH_3

471 and HNO_3 were calculated in this study. More details regarding the calculation steps

472 of the above factors can be found in section 2.4. Based on the thermodynamic

473 principles presented by Stelson and Seinfeld (1982), when the product of the partial

474 pressures of NH_3 and HNO_3 ($P_{HNO3} \times P_{NH3}$) is greater than Kp, the equilibrium of the

475 system shifts toward the aerosol phase, thus increasing NH_4NO_3 formation. In

476 contrast, a relatively low $P_{HNO3} \times P_{NH3}$/Kp value (<1) suggests that NH_4NO_3

477 dissociation is induced and that NH_4NO_3 is transferred to the gas phase. Figure 9

478 depicts the ratio of the product of the partial pressures of NH_3 and HNO_3 with

479 different ambient temperatures. As shown in Figure 9, approximately 85% of the

480 samples collected at both sampling sites were located within the region with

481 $P_{HNO3} \times P_{NH3}$/Kp less than 1, demonstrating a common NH_4NO_3 dissociation

482 phenomenon during the observed period. For the samples with $P_{HNO3} \times P_{NH3}$/Kp ratios

483 <1, the mean value of the MS-site ratios was approximately half that of the MF-site

484 ratios, indicating that NH_4NO_3 dissociation may be more likely at higher elevations

485 than that at lower elevations. This finding was inconsistent with the aircraft

486 observations of the wildfire smoke plumes collected by Lindaas et al. (2021), who

487 revealed that $P_{HNO3} \times P_{NH3}$/Kp exhibited an increasing trend within 1-3 km (a.s.l.). As

488 we know, the abundant NH_3 and NOx can be emitted by the wildfire, which would be

489 transported aloft and lead to a higher NH_3 and HNO_3 mixing ratio compared to that at

490   lower elevation. This may drive a higher $P_{HNO3} \times P_{NH3}/K_p$ ratio at the upper layers of

491   aircraft observations in the western U.S. (Lindaas et al., 2021).

492   Moreover, the nitrogen isotope compositions of nitrate and ammonium in $PM_{2.5}$

493   that can retain invaluable information regarding physicochemical processes

494   (Wiedenhaus et al., 2021; Elliott et al., 2019), were thus measured to further verify the

495   conceptual model. As previously mentioned, unlike daytime pollutants, nocturnal

496   pollutants exhibited different sources between the two sampling sites. Thus, their

497   nitrogen isotope compositions were more complicated and less comparable. However,

498   for simplicity, only the daytime samples were analyzed herein based on the hypothesis

499   that the sources of the high-elevation pollutants were the same as those of the

500   pollutants collected at the MF site. As shown in Figure 10, a discrepancy in the $\delta^{15}N$

501   value of nitrate ($\delta^{15}N\text{-}NO_3^-$) featuring more ^{15}N-enriched NO_3^- was observed at the

502   MS site, with a p value less than 0.05. This finding can be ascribed to the evaporation

503   of a portion of the particulate NH_4NO_3 due to a dissociation shift in equilibrium; in

504   this shift, the lighter ^{14}N was preferentially incorporated into the atmosphere, leading

505   to ^{15}N enrichment in the remaining nitrate. Similar phenomenon was also revealed by

506   Wiedenhaus et al. (2021), who thought that the ammonium nitrate dissociation may be

507   an important reason for the accumulation of ^{15}N in aerosol particles. Additionally,

508   Freyer et al. (1993) revealed that gas-phase isotopic exchanges between NO and NO_2

509   result in the enrichment of the heavier ^{15}N isotope in the more oxidized form and may

510   further affect $\delta^{15}N\text{-}NO_3^-$ through nitrate formation reactions. The above isotopic

511   exchange between NO_2 and NOx can be roughly described as follows: $[\delta^{15}N(NO_2)\text{-}$

512　$\delta^{15}N(NOx)]=(1- K)\times(1-f_{NO2})$, where K and f_{NO2} are the temperature-dependent

513　exchange constant and mole fraction of NO_2, respectively. Based on trace gas

514　observations, the f_{NO2} values of the air aloft were very high due to the frequently

515　undetectable NO concentration, indicating a rather limited isotopic exchange between

516　NO_2 and NO. Therefore, the evaporation of particulate NH_4NO_3 have been the

517　significant factor affecting the measurement of a higher $\delta^{15}N\text{-}NO_3^-$ at the MS site than

518　at the MF site in our observations. According to the above analysis, the ammonium at

519　MS site should theoretically be more and more enriched in $\delta^{15}N$ with the continuous

520　NH_4NO_3 volatilization. However, our observation of $\delta^{15}N\text{-}NH_4^+$ did not correspond to

521　above pattern, namely, ammonium at the MS site depleted in $\delta^{15}N$ compared to that at

522　MF site ($p<0.05$, Figure 10). Given the unchanged NH_3 sources as verified in section

523　3.1.2, such seemingly unreasonable observations were mainly caused by the gas-to-

524　particle conversion of ammonia. In this process, the reversible phase-equilibrium

525　reactions between $NH_3(g)$ and $HNO_3(g)/HCl(g)$ would yield positive enrichment in

526　$\delta^{15}N$ of aerosol NH_4^+ (Walters et al., 2019); nevertheless, unidirectional reactions

527　involving $NH_3(g)$ and SO_4^{2-}/HSO_4^- favored ^{15}N depletion in the particle form as

528　revealed by Heaton et al. (1997). Thereby, the lower $\delta^{15}N\text{-}NH_4^+$ values at MS site

529　were mostly driven by those irreversible reactions, rather than the reversible

530　equilibrium ones. This result further confirmed our conjecture that the additional NH_3

531　would partition into particulate phases and further neutralize the acidic NH_4HSO_4,

532　leading to an increasing pH at MS site compared to that at MF site. Taken together,

533　this compelling evidence verifies that fine-mode nitrate and ammonium exhibit

534   distinctly different physicochemical behaviors during their transport.

535   **4 Conclusions and atmospheric implications**

536   In this study, aerosol samples were collected at 4-hr intervals on the mountainside

537   of Mt. Hua, and the OC, EC, water-soluble ions and isotope compositions of nitrate

538   and ammonium were measured and compared with simultaneous observations taken

539   at a lower-elevation site (MF site). The particle mass at the MF site was

540   approximately 1.5-fold that at the MS site, and distinctly different diurnal cycles were

541   observed between the two sampling sites. Based on the BLH variation, we revealed

542   that near-surface $PM_{2.5}$ could be transported to the upper layers by the mountain-

543   valley breeze, leading to the gradual accumulation of pollutants on the mountainside

544   during the daytime.

545   Sulfate, the predominant species found among ions at both sampling sites,

546   exhibited nearly identical mass concentrations at the two sites but had a moderately

547   enhanced mass fraction at MS site. Such homogeneity was also observed in

548   ammonium, which mainly existed as $NH_4HSO_4+NH_4NO_3$ and $(NH_4)_2SO_4+NH_4NO_3$ at

549   the MF and MS sites, respectively. This observation indicated the further formation of

550   ammonium during the transport process. Unlike sulfate and ammonium, nitrate at the

551   MS site exhibited abated trends in both its concentration and proportion, mainly due

552   to the volatilization of NH_4NO_3. With the help of nitrate and ammonium nitrogen

553   isotopes, we proposed a conceptual model to illustrate the different behaviors of

554   nitrate and ammonium during vertical transport; in this model, the semivolatile

555   NH_4NO_3 in surface air parcels was easily converted into gaseous NH_3 and HNO_3.

556 Subsequently, heterogeneous reactions occurred between this gaseous HNO_3 and

557 fugitive dust, forming nonvolatile salts and leading to a significant nitrate shift from

558 fine particles into coarse particles. In addition, the decreasing temperature was

559 favorable for NH_3 partitioning toward the particle phase, and the addition of

560 ammonium further neutralized HSO_4^- to form SO_4^{2-}. This process would reduce the

561 aerosol acidity, with bulk $PM_{2.5}$ pH increasing from 2.9±2.0 at MF site to 3.4±2.2 at

562 MS site.

563 Over the past decade, the relative abundance of NH_4NO_3 has been enhanced in

564 most urban areas of China because strict emission directives have been promulgated

565 to abate the emission and environmental impacts of SO_2 (Xie et al., 2020; Song et al.,

566 2019). In this work, we observed that NH_4NO_3 volatilization was a ubiquitous

567 phenomenon for particles during transport, resulting in a shift in partwise nitrate from

568 the fine mode to the coarse fraction; this shift has also been reported in the offshore

569 areas of the UK (Yeatman et al., 2001). Thus, we think that considering only fine-

570 fraction nitrate may result in the conversion rate of NOx to nitrate being partly

571 underestimated at some times, especially in the summer. Moreover, the deposition

572 velocity of coarse particles is usually faster than that of fine particles; therefore, the

573 above process would appreciably elevate the deposition of N into the environment.

574 Indeed, abundant NO_2, O_3 and NH_3 co-occurrence is common in the East Asian

575 atmosphere, and under these conditions, secondary inorganic aerosols can be

576 effectively produced, leading to a $PM_{2.5}$ loading explosion in the urban atmosphere of

577 China (Wu et al., 2020c; Wang et al., 2016). Given this, harmonious reductions in

578 NO$_2$, O$_3$ and NH$_3$ will be urgent in further mitigation strategies to improve air quality

579 and alleviate other potential effects.

580

581 **Author contributions.** GW designed the experiment. CW, JiaL and CC collected the

582 samples. CW and CC conducted the experiments. CW and GW performed the data

583 interpretation and wrote the paper. All authors contributed to the paper with useful

584 scientific discussions or comments.

585

586 **Competing interests.** The authors declare that they have no conflict of interest.

587

594
595
596

597 **References**

598 Andreae, M. O. and Ramanathan, V.: Climate's Dark Forcings, Science, 340, 280-281,
599   10.1126/science.1235731, 2013.
600 Baasandorj, M., Hoch, S. W., Bares, R., Lin, J. C., Brown, S. S., Millet, D. B., Martin, R., Kelly, K.,
601   Zarzana, K. J., Whiteman, C. D., Dube, W. P., Tonnesen, G., Jaramillo, I. C., and Sohl, J.: Coupling
602   between Chemical and Meteorological Processes under Persistent Cold-Air Pool Conditions:
603   Evolution of Wintertime PM2.5 Pollution Events and N2O5 Observations in Utah's Salt Lake Valley,
604   Environ. Sci. Technol., 51, 5941-5950, 10.1021/acs.est.6b06603, 2017.
605 Bond, T. C., Doherty, S. J., Fahey, D. W., Forster, P. M., Berntsen, T., DeAngelo, B. J., Flanner, M. G.,

Ghan, S., Kaercher, B., Koch, D., Kinne, S., Kondo, Y., Quinn, P. K., Sarofim, M. C., Schultz, M. G., Schulz, M., Venkataraman, C., Zhang, H., Zhang, S., Bellouin, N., Guttikunda, S. K., Hopke, P. K., Jacobson, M. Z., Kaiser, J. W., Klimont, Z., Lohmann, U., Schwarz, J. P., Shindell, D., Storelvmo, T., Warren, S. G., and Zender, C. S.: Bounding the role of black carbon in the climate system: A scientific assessment, J. Geophys. Res.-Atmos., 118, 5380-5552, 10.1002/jgrd.50171, 2013.

Carslaw, K. S., Lee, L. A., Reddington, C. L., Pringle, K. J., Rap, A., Forster, P. M., Mann, G. W., Spracklen, D. V., Woodhouse, M. T., Regayre, L. A., and Pierce, J. R.: Large contribution of natural aerosols to uncertainty in indirect forcing, Nat., 503, 67-+, 10.1038/nature12674, 2013.

Dzepina, K., Mazzoleni, C., Fialho, P., China, S., Zhang, B., Owen, R. C., Helmig, D., Hueber, J., Kumar, S., Perlinger, J. A., Kramer, L. J., Dziobak, M. P., Ampadu, M. T., Olsen, S., Wuebbles, D. J., and Mazzoleni, L. R.: Molecular characterization of free tropospheric aerosol collected at the Pico Mountain Observatory: a case study with a long-range transported biomass burning plume, Atmos. Chem. Phys., 15, 5047-5068, 10.5194/acp-15-5047-2015, 2015.

Elliott, E. M., Yu, Z., Cole, A. S., and Coughlin, J. G.: Isotopic advances in understanding reactive nitrogen deposition and atmospheric processing, Sci. Total Environ., 662, 393-403, 10.1016/j.scitotenv.2018.12.177, 2019.

Fan, J., Rosenfeld, D., Zhang, Y., Giangrande, S. E., Li, Z., Machado, L. A. T., Martin, S. T., Yang, Y., Wang, J., Artaxo, P., Barbosa, H. M. J., Braga, R. C., Comstock, J. M., Feng, Z., Gao, W., Gomes, H. B., Mei, F., Poehlker, C., Poehlker, M. L., Poeschl, U., and de Souza, R. A. F.: Substantial convection and precipitation enhancements by ultrafine aerosol particles, Science, 359, 411-+, 10.1126/science.aan8461, 2018.

Fan, M.-Y., Zhang, Y.-L., Lin, Y.-C., Hong, Y., Zhao, Z.-Y., Xie, F., Du, W., Cao, F., Sun, Y., and Fu, P.: Important Role of NO3 Radical to Nitrate Formation Aloft in Urban Beijing: Insights from Triple Oxygen Isotopes Measured at the Tower, Environ. Sci. Technol., 10.1021/acs.est.1c02843, 2021.

Fang, Y. T., Koba, K., Wang, X. M., Wen, D. Z., Li, J., Takebayashi, Y., Liu, X. Y., and Yoh, M.: Anthropogenic imprints on nitrogen and oxygen isotopic composition of precipitation nitrate in a nitrogen-polluted city in southern China, Atmos. Chem. Phys., 11, 1313-1325, 10.5194/acp-11-1313-2011, 2011.

Ferrero, L., Cappelletti, D., Moroni, B., Sangiorgi, G., Perrone, M. G., Crocchianti, S., and Bolzacchini, E.: Wintertime aerosol dynamics and chemical composition across the mixing layer over basin valleys, Atmos. Environ., 56, 143-153, 10.1016/j.atmosenv.2012.03.071, 2012.

Freyer, H. D., Kley, D., Volz-Thomas, A., and Kobel, K.: On the interaction of isotopic exchange processes with photochemical reactions in atmospheric oxides of nitrogen, Journal of Geophysical Research, 98, 14791-14796, 10.1029/93jd00874, 1993.

Fuzzi, S., Baltensperger, U., Carslaw, K., Decesari, S., van der Gon, H. D., Facchini, M. C., Fowler, D., Koren, I., Langford, B., Lohmann, U., Nemitz, E., Pandis, S., Riipinen, I., Rudich, Y., Schaap, M., Slowik, J. G., Spracklen, D. V., Vignati, E., Wild, M., Williams, M., and Gilardoni, S.: Particulate matter, air quality and climate: lessons learned and future needs, Atmos. Chem. Phys., 15, 8217-8299, 10.5194/acp-15-8217-2015, 2015.

Guo, S., Hu, M., Zamora, M. L., Peng, J., Shang, D., Zheng, J., Du, Z., Wu, Z., Shao, M., Zeng, L., Molina, M. J., and Zhang, R.: Elucidating severe urban haze formation in China, Proc. Natl. Acad. Sci. USA, 111, 17373-17378, 10.1073/pnas.1419604111, 2014.

Harrison, R. M. and Pio, C. A.: Size-differentiated composition of inorganic atmospheric aerosols of both marine and polluted continental origin, Atmos. Environ., 17, 1733-1738, 10.1016/0004-

6981(83)90180-4, 1983.

Heaton, T. H. E., Spiro, B., Madeline, S., and Robertson, C.: Potential canopy influences on the isotopic composition of nitrogen and sulphur in atmospheric deposition, Oecologia, 109, 600-607, 10.1007/s004420050122, 1997.

Lambey, V. and Prasad, A. D.: A Review on Air Quality Measurement Using an Unmanned Aerial Vehicle, Water, Air, & Soil Pollution, 232, 10.1007/s11270-020-04973-5, 2021.

Lelieveld, J., Evans, J. S., Fnais, M., Giannadaki, D., and Pozzer, A.: The contribution of outdoor air pollution sources to premature mortality on a global scale, Nat., 525, 367-+, 10.1038/nature15371, 2015.

Li, D., Wu, C., Zhang, S., Lei, Y., Lv, S., Du, W., Liu, S., Zhang, F., Liu, X., Liu, L., Meng, J., Wang, Y., Gao, J., and Wang, G.: Significant coal combustion contribution to water-soluble brown carbon during winter in Xingtai, China: Optical properties and sources, J. Environ. Sci., 124, 892-900, 10.1016/j.jes.2022.02.026, 2023.

Li, J. J., Wang, G. H., Cao, J. J., Wang, X. M., and Zhang, R. J.: Observation of biogenic secondary organic aerosols in the atmosphere of a mountain site in central China: temperature and relative humidity effects, Atmos. Chem. Phys., 13, 11535-11549, 10.5194/acp-13-11535-2013, 2013.

Li, T., Wang, Y., Li, W. J., Chen, J. M., Wang, T., and Wang, W. X.: Concentrations and solubility of trace elements in fine particles at a mountain site, southern China: regional sources and cloud processing, Atmos. Chem. Phys., 15, 8987-9002, 10.5194/acp-15-8987-2015, 2015.

Li, W., Shao, L., Zhang, D., Ro, C.-U., Hu, M., Bi, X., Geng, H., Matsuki, A., Niu, H., and Chen, J.: A review of single aerosol particle studies in the atmosphere of East Asia: morphology, mixing state, source, and heterogeneous reactions, Journal of Cleaner Production, 112, 1330-1349, 10.1016/j.jclepro.2015.04.050, 2016.

Lindaas, J., Pollack, I. B., Calahorrano, J. J., O'Dell, K., Garofalo, L. A., Pothier, M. A., Farmer, D. K., Kreidenweis, S. M., Campos, T., Flocke, F., Weinheimer, A. J., Montzka, D. D., Tyndall, G. S., Apel, E. C., Hills, A. J., Hornbrook, R. S., Palm, B. B., Peng, Q., Thornton, J. A., Permar, W., Wielgasz, C., Hu, L., Pierce, J. R., Collett, J. L., Jr., Sullivan, A. P., and Fischer, E. V.: Empirical Insights Into the Fate of Ammonia in Western US Wildfire Smoke Plumes, J. Geophys. Res.-Atmos., 126, 10.1029/2020jd033730, 2021.

Liu, D., Fang, Y., Tu, Y., and Pan, Y.: Chemical Method for Nitrogen Isotopic Analysis of Ammonium at Natural Abundance, Anal. Chem., 86, 3787-3792, 10.1021/ac403756u, 2014.

Liu, L. J. S., Burton, R., Wilson, W. E., and Koutrakis, P.: Comparison of aerosol acidity in urban and semirural environments, Atmos. Environ., 30, 1237-1245, 10.1016/1352-2310(95)00438-6, 1996.

Liu, T., Chan, A. W. H., and Abbatt, J. P. D.: Multiphase Oxidation of Sulfur Dioxide in Aerosol Particles: Implications for Sulfate Formation in Polluted Environments, Environ. Sci. Technol., 55, 4227-4242, 10.1021/acs.est.0c06496, 2021.

Lv, D., Chen, Y., Zhu, T., Li, T., Shen, F., Li, X., and Mehmood, T.: The pollution characteristics of PM10 and PM2.5 during summer and winter in Beijing, Suning and Islamabad, Atmospheric Pollution Research, 10, 1159-1164, 10.1016/j.apr.2019.01.021, 2019.

Lv, S., Wang, F., Wu, C., Chen, Y., Liu, S., Zhang, S., Li, D., Du, W., Zhang, F., Wang, H., Huang, C., Fu, Q., Duan, Y., and Wang, G.: Gas-to-Aerosol Phase Partitioning of Atmospheric Water-Soluble Organic Compounds at a Rural Site in China: An Enhancing Effect of NH3 on SOA Formation, Environ. Sci. Technol., 56, 3915-3924, 10.1021/acs.est.1c06855, 2022.

Meng, J., Wang, G., Hou, Z., Liu, X., Wei, B., Wu, C., Cao, C., Wang, J., Li, J., Cao, J., Zhang, E., Dong,

J., Liu, J., Ge, S., and Xie, Y.: Molecular distribution and stable carbon isotopic compositions of dicarboxylic acids and related SOA from biogenic sources in the summertime atmosphere of Mt. Tai in the North China Plain, Atmos. Chem. Phys., 18, 15069-15086, 10.5194/acp-18-15069-2018, 2018.

Mozurkewich, M.: The dissociation constant of ammonium nitrate and its dependence on temperature, relative humidity and particle size, Atmospheric Environment. Part A. General Topics, 27, 261-270, 1993.

Nault, B. A., Campuzano-Jost, P., Day, D. A., Jo, D. S., Schroder, J. C., Allen, H. M., Bahreini, R., Bian, H., Blake, D. R., Chin, M., Clegg, S. L., Colarco, P. R., Crounse, J. D., Cubison, M. J., DeCarlo, P. F., Dibb, J. E., Diskin, G. S., Hodzic, A., Hu, W., Katich, J. M., Kim, M. J., Kodros, J. K., Kupc, A., Lopez-Hilfiker, F. D., Marais, E. A., Middlebrook, A. M., Andrew Neuman, J., Nowak, J. B., Palm, B. B., Paulot, F., Pierce, J. R., Schill, G. P., Scheuer, E., Thornton, J. A., Tsigaridis, K., Wennberg, P. O., Williamson, C. J., and Jimenez, J. L.: Chemical transport models often underestimate inorganic aerosol acidity in remote regions of the atmosphere, Communications Earth & Environment, 2, 10.1038/s43247-021-00164-0, 2021.

Pakkanen, T. A.: Study of formation of coarse particle nitrate aerosol, Atmos. Environ., 30, 2475-2482, 10.1016/1352-2310(95)00492-0, 1996.

Petit, J. E., Favez, O., Albinet, A., and Canonaco, F.: A user-friendly tool for comprehensive evaluation of the geographical origins of atmospheric pollution: Wind and trajectory analyses, Environmental Modelling & Software, 88, 183-187, 10.1016/j.envsoft.2016.11.022, 2017.

Raes, F., Van Dingenen, R., Vignati, E., Wilson, J., Putaud, J. P., Seinfeld, J. H., and Adams, P.: Formation and cycling of aerosols in the global troposphere, Atmos. Environ., 34, 4215-4240, 10.1016/s1352-2310(00)00239-9, 2000.

Reid, J. S., Kuehn, R. E., Holz, R. E., Eloranta, E. W., Kaku, K. C., Kuang, S., Newchurch, M. J., Thompson, A. M., Trepte, C. R., Zhang, J., Atwood, S. A., Hand, J. L., Holben, B. N., Minnis, P., and Posselt, D. J.: Ground-based High Spectral Resolution Lidar observation of aerosol vertical distribution in the summertime Southeast United States, J. Geophys. Res.-Atmos., 122, 2970-3004, 10.1002/2016jd025798, 2017.

rganization, W. H.: WHO global air quality guidelines: particulate matter (PM2. 5 and PM10), ozone, nitrogen dioxide, sulfur dioxide and carbon monoxide, World Health Organization2021.

Rodhe, H., Crutzen, P., and Vanderpol, A.: Formation of sulfuric and nitric acid in the atmosphere during long-range transport, Tellus, 33, 132-141, 1981.

Seinfeld and JohnH: Atmospheric chemistry and physics : from air pollution to climate change / 3nd ed, Atmospheric chemistry and physics : from air pollution to climate change / 3nd ed2016.

Shi, Q., Davidovits, P., Jayne, J. T., Worsnop, D. R., and Kolb, C. E.: Uptake of gas-phase ammonia. 1. Uptake by aqueous surfaces as a function of pH, J. Phys. Chem. A, 103, 8812-8823, 10.1021/jp991696p, 1999.

Shiraiwa, M., Ueda, K., Pozzer, A., Lammel, G., Kampf, C. J., Fushimi, A., Enami, S., Arangio, A. M., Froehlich-Nowoisky, J., Fujitani, Y., Furuyama, A., Lakey, P. S. J., Lelieveld, J., Lucas, K., Morino, Y., Poeschl, U., Takaharna, S., Takami, A., Tong, H., Weber, B., Yoshino, A., and Sato, K.: Aerosol Health Effects from Molecular to Global Scales, Environ. Sci. Technol., 51, 13545-13567, 10.1021/acs.est.7b04417, 2017.

Song, S., Nenes, A., Gao, M., Zhang, Y., Liu, P., Shao, J., Ye, D., Xu, W., Lei, L., Sun, Y., Liu, B., Wang, S., and McElroy, M. B.: Thermodynamic Modeling Suggests Declines in Water Uptake and Acidity

of Inorganic Aerosols in Beijing Winter Haze Events during 2014/2015-2018/2019, Environmental Science & Technology Letters, 6, 752-760, 10.1021/acs.estlett.9b00621, 2019.

Stelson, A. W. and Seinfeld, J. H.: Relative humidity and temperature dependence of the ammonium nitrate dissociation constant, Atmos. Environ., 16, 983-992, 10.1016/0004-6981(82)90184-6, 1982.

Tang, I. N. and Munkelwitz, H. R.: Composition and temperature dependence of the deliquescence properties of hygroscopic aerosols, Atmos. Environ., 27, 467-473, 1993.

van Donkelaar, A., Martin, R. V., Brauer, M., Hsu, N. C., Kahn, R. A., Levy, R. C., Lyapustin, A., Sayer, A. M., and Winker, D. M.: Global Estimates of Fine Particulate Matter using a Combined Geophysical-Statistical Method with Information from Satellites, Models, and Monitors, Environ. Sci. Technol., 50, 3762-3772, 10.1021/acs.est.5b05833, 2016.

Walters, W. W., Chai, J., and Hastings, M. G.: Theoretical Phase Resolved Ammonia-Ammonium Nitrogen Equilibrium Isotope Exchange Fractionations: Applications for Tracking Atmospheric Ammonia Gas-to-Particle Conversion, ACS Earth Space Chem., 3, 79-89, 10.1021/acsearthspacechem.8b00140, 2019.

Wang, G., Kawamura, K., Hatakeyama, S., Takami, A., Li, H., and Wang, W.: Aircraft measurement of organic aerosols over China, Environ. Sci. Technol., 41, 3115-3120, 10.1021/es062601h, 2007.

Wang, G., Kawamura, K., Xie, M., Hu, S., Gao, S., Cao, J., An, Z., and Wang, Z.: Size-distributions of n-alkanes, PAHs and hopanes and their sources in the urban, mountain and marine atmospheres over East Asia, Atmos. Chem. Phys., 9, 8869-8882, 10.5194/acp-9-8869-2009, 2009.

Wang, G., Kawamura, K., Xie, M., Hu, S., Li, J., Zhou, B., Cao, J., and An, Z.: Selected water-soluble organic compounds found in size-resolved aerosols collected from urban, mountain and marine atmospheres over East Asia, Tellus Series B-Chemical and Physical Meteorology, 63, 371-381, 10.1111/j.1600-0889.2011.00536.x, 2011.

Wang, G., Zhang, R., Gomez, M. E., Yang, L., Zamora, M. L., Hu, M., Lin, Y., Peng, J., Guo, S., Meng, J., Li, J., Cheng, C., Hu, T., Ren, Y., Wang, Y., Gao, J., Cao, J., An, Z., Zhou, W., Li, G., Wang, J., Tian, P., Marrero-Ortiz, W., Secrest, J., Du, Z., Zheng, J., Shang, D., Zeng, L., Shao, M., Wang, W., Huang, Y., Wang, Y., Zhu, Y., Li, Y., Hu, J., Pan, B., Cai, L., Cheng, Y., Ji, Y., Zhang, F., Rosenfeld, D., Liss, P. S., Duce, R. A., Kolb, C. E., and Molina, M. J.: Persistent sulfate formation from London Fog to Chinese haze, Proc. Natl. Acad. Sci. USA, 113, 13630-13635, 10.1073/pnas.1616540113, 2016.

Wang, G. H., Zhou, B. H., Cheng, C. L., Cao, J. J., Li, J. J., Meng, J. J., Tao, J., Zhang, R. J., and Fu, P. Q.: Impact of Gobi desert dust on aerosol chemistry of Xi'an, inland China during spring 2009: differences in composition and size distribution between the urban ground surface and the mountain atmosphere, Atmos. Chem. Phys., 13, 819-835, 10.5194/acp-13-819-2013, 2013.

Wankel, S. D., Chen, Y., Kendall, C., Post, A. F., and Paytan, A.: Sources of aerosol nitrate to the Gulf of Aqaba: Evidence from delta N-15 and delta O-18 of nitrate and trace metal chemistry, Mar. Chem., 120, 90-99, 10.1016/j.marchem.2009.01.013, 2010.

Wexler, A. S. and Seinfeld, J. H.: Second-generation inorganic aerosol model, Atmos. Environ., 25A, 2731-2748, 1991.

Wiedenhaus, H., Ehrnsperger, L., Klemm, O., and Strauss, H.: Stable N-15 isotopes in fine and coarse urban particulate matter, Aerosol Sci. Technol., 55, 859-870, 10.1080/02786826.2021.1905150, 2021.

Wu, C., Liu, L., Wang, G., Zhang, S., Li, G., Lv, S., Li, J., Wang, F., Meng, J., and Zeng, Y.: Important contribution of N2O5 hydrolysis to the daytime nitrate in Xi'an, China during haze periods: Isotopic

782   analysis and WRF-Chem model simulation, Environmental pollution (Barking, Essex : 1987), 288,
783   117712-117712, 10.1016/j.envpol.2021.117712, 2021.

784 Wu, C., Wang, G., Li, J., Li, J., Cao, C., Ge, S., Xie, Y., Chen, J., Liu, S., Du, W., Zhao, Z., and Cao, F.:
785   Non-agricultural sources dominate the atmospheric NH3 in Xi'an, a megacity in the semi-arid region
786   of China, Sci. Total Environ., 722, 137756, 10.1016/j.scitotenv.2020.137756, 2020a.

787 Wu, C., Wang, G., Li, J., Li, J., Cao, C., Ge, S., Xie, Y., Chen, J., Li, X., Xue, G., Wang, X., Zhao, Z.,
788   and Cao, F.: The characteristics of atmospheric brown carbon in Xi'an, inland China: sources, size
789   distributions and optical properties, Atmos. Chem. Phys., 20, 2017-2030, 10.5194/acp-20-2017-
790   2020, 2020b.

791 Wu, C., Zhang, S., Wang, G., Lv, S., Li, D., Liu, L., Li, J., Liu, S., Du, W., Meng, J., Qiao, L., Zhou, M.,
792   Huang, C., and Wang, H.: Efficient Heterogeneous Formation of Ammonium Nitrate on the Saline
793   Mineral Particle Surface in the Atmosphere of East Asia during Dust Storm Periods, Environ. Sci.
794   Technol., 54, 15622-15630, 10.1021/acs.est.0c04544, 2020c.

795 Xie, Y., Wang, G., Wang, X., Chen, J., Chen, Y., Tang, G., Wang, L., Ge, S., Xue, G., Wang, Y., and Gao,
796   J.: Nitrate-dominated PM2.5 and elevation of particle pH observed in urban Beijing during the
797   winter of 2017, Atmos. Chem. Phys., 20, 5019-5033, 10.5194/acp-20-5019-2020, 2020.

798 Xu, Z., Huang, X., Nie, W., Shen, Y., Zheng, L., Xie, Y., Wang, T., Ding, K., Liu, L., Zhou, D., Qi, X.,
799   and Ding, A.: Impact of Biomass Burning and Vertical Mixing of Residual-Layer Aged Plumes on
800   Ozone in the Yangtze River Delta, China: A Tethered-Balloon Measurement and Modeling Study of
801   a Multiday Ozone Episode, J. Geophys. Res.-Atmos., 123, 11786-11803, 10.1029/2018jd028994,
802   2018.

803 Yeatman, S. G., Spokes, L. J., Dennis, P. F., and Jickells, T. D.: Can the study of nitrogen isotopic
804   composition in size-segregated aerosol nitrate and ammonium be used to investigate atmospheric
805   processing mechanisms?, Atmos. Environ., 35, 1337-1345, 10.1016/s1352-2310(00)00457-x, 2001.

806 Yi, Y., Meng, J., Hou, Z., Wang, G., Zhou, R., Li, Z., Li, Y., Chen, M., Liu, X., Li, H., and Yan, L.:
807   Contrasting compositions and sources of organic aerosol markers in summertime PM(2.5)from
808   urban and mountainous regions in the North China Plain, Sci. Total Environ., 766,
809   10.1016/j.scitotenv.2020.144187, 2021.

810 Zhang, Y., Forrister, H., Liu, J., Dibb, J., Anderson, B., Schwarz, J. P., Perring, A. E., Jimenez, J. L.,
811   Campuzano-Jost, P., Wang, Y., Nenes, A., and Weber, R. J.: Top-of-atmosphere radiative forcing
812   affected by brown carbon in the upper troposphere, Nat. Geosci., 10, 486-+, 10.1038/ngeo2960,
813   2017.

814 Zheng, B., Tong, D., Li, M., Liu, F., Hong, C., Geng, G., Li, H., Li, X., Peng, L., Qi, J., Yan, L., Zhang,
815   Y., Zhao, H., Zheng, Y., He, K., and Zhang, Q.: Trends in China's anthropogenic emissions since
816   2010 as the consequence of clean air actions, Atmos. Chem. Phys., 18, 14095-14111, 10.5194/acp-
817   18-14095-2018, 2018.

818 Zhou, S., Wu, L., Guo, J., Chen, W., Wang, X., Zhao, J., Cheng, Y., Huang, Z., Zhang, J., Sun, Y., Fu, P.,
819   Jia, S., Tao, J., Chen, Y., and Kuang, J.: Measurement report: Vertical distribution of atmospheric
820   particulate matter within the urban boundary layer in southern China - size-segregated chemical
821   composition and secondary formation through cloud processing and heterogeneous reactions,
822   Atmos. Chem. Phys., 20, 6435-6453, 10.5194/acp-20-6435-2020, 2020.

823 Zhou, Y., Hakala, S., Yan, C., Gao, Y., Yao, X., Chu, B., Chan, T., Kangasluoma, J., Gani, S., Kontkanen,
824   J., Paasonen, P., Liu, Y., Petaja, T., Kulmala, M., and Dada, L.: Measurement report: New particle
825   formation characteristics at an urban and a mountain station in northern China, Atmos. Chem. Phys.,

826   21, 17885-17906, 10.5194/acp-21-17885-2021, 2021.

827
828
829
830
831

832   **Table caption**

833   Table 1 Mass concentrations of species in the PM$_{2.5}$ samples and the meteorological
834   conditions at the two sampling sites.

835
836
837

838   **Figure captions**

839

840   Figure 1 (a) Location of the study sites in China, (b) topographic view of Mt. Hua
841   with the sampling sites mark, and (c) vertical views of the two sampling sites and the
842   horizontal distance between them. (The maps are produced by mapbox,
843   https://account.mapbox.com/, last access, 31 Dec. 2021).

844

845   Figure 2 Time series of the temperature (T), relative humidity (RH), boundary layer
846   height (BLH) and mass concentrations of PM$_{2.5}$ and the water-soluble ions in PM$_{2.5}$
847   during the observation period at the two sampling sites.

848

849   Figure 3 Diurnal variations in PM$_{2.5}$ and the boundary layer height (BLH) at the
850   different observation sites.

851

852   Figure 4 Concentration-weighted trajectory (CWT) analyses of PM$_{2.5}$ in both the
853   daytime (8:00-20:00) and nighttime (21:00-7:00) at the MS site.

854

855   Figure 5 The distribution of averaged diurnal divergence over the whole campaign, with

856   corresponding wind filed. (a) Horizontal distribution at surface. (b) Longitude-pressure

857   cross-sections at 34°29′N. Wind speeds were represented by arrows sizes, and the W

858   component of wind vectors was magnified 10 times.

859

860   Figure 6 Mass closure of PM$_{2.5}$ during the observed period (OM=1.6×OC).

861

862   Figure 7 Comparison of the calculated and observed NH$_4^+$ concentrations at the MF
863   and MS sampling sites.

864

865   Figure 8 Schematic of the physicochemical behaviors of nitrate and ammonium during
866   the transport process.

867

868 Figure 9 Temperature dependence of the ratio of the product of the partial pressures of
869 NH_3 and HNO_3 with the dry dissociation constant of NH_4NO_3.

870

871 Figure 10 Nitrate and ammonium $\delta^{15}N$ values at the two sampling sites in the daytime.

872
873
874
875
876
877
878
879 Table 1 Mass concentrations of species in the $PM_{2.5}$ samples, pH and the
880 meteorological conditions at the two sampling sites.

	Mountain foot	Mountainside
(i) Mass concentration of species and ALWC ($\mu g/m^3$) and pH		
SO_4^{2-}	10.1±6.4	9.0±7.1
NO_3^-	6.1±6.3	3.8±5.8
NH_4^+	3.9±3.3	3.9±3.5
Cl^-	0.4±0.5	0.37±0.50
Na^+	0.70±0.8	0.47±0.62
K^+	0.2±0.3	0.37±0.5
Mg^{2+}	0.1±0.1	0.07±0.06
Ca^{2+}	2.5±2.0	0.9±1.2
OC	14.0±4.7	5.0±2.8
EC	4.3±2.0	1.1±0.7
$PM_{2.5}$	76.0±44.1	47.0±38.0
ALWC	27.6±63.9	26.9±71.4
pH	3.4±2.2	2.9±2.0
(ii) Meteorological parameters		
T (°C)	23.2±4.2	15.0±2.5
RH (%)	68.9±18.2	62.8±20.0
Wind speed (m/s)	1.3±1.1	3.2±2.0
Visibility (km)	14.1±9.5	22.2±12.1

881 ALWC and pH are predicted by the thermodynamic model (E-AIM (IV))

882
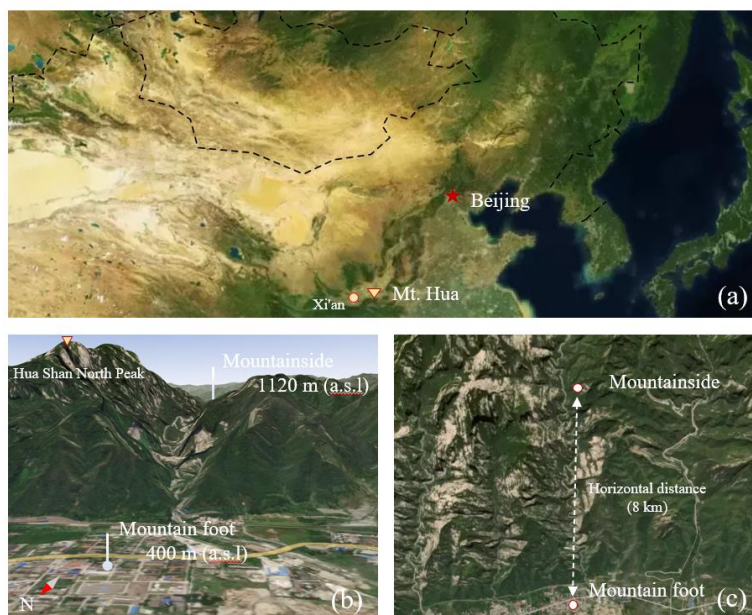
883

Figure 1 (a) Location of the study sites in China, (b) topographic view of Mt. Hua
with the sampling sites mark, and (c) vertical views of the two sampling sites and the
horizontal distance between them. (The maps are produced by mapbox,
https://account.mapbox.com/, last access, 31 Dec. 2021).

888

889

890
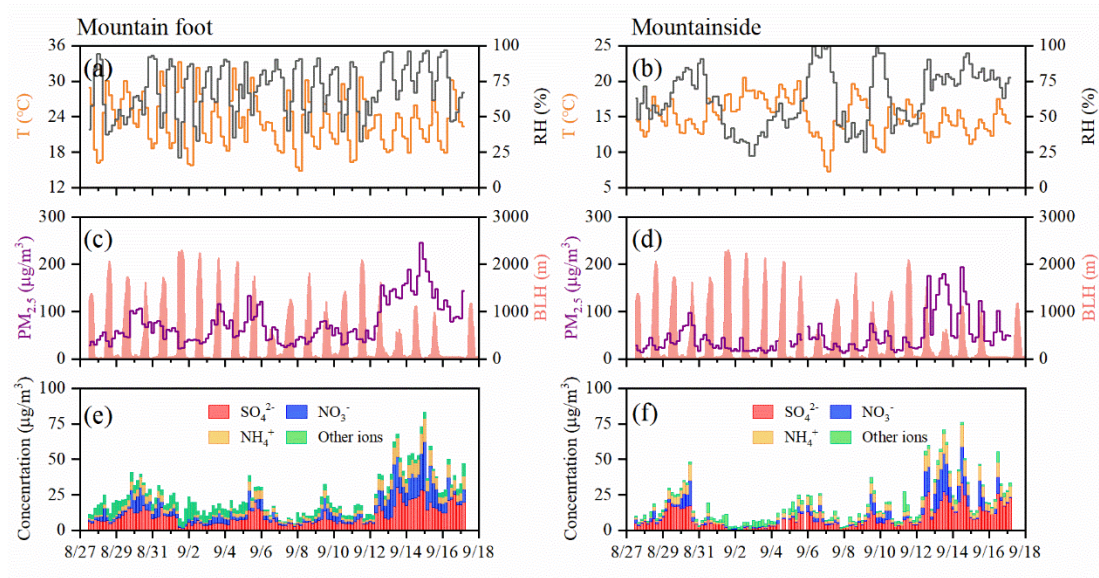
891

Figure 2 Time series of the temperature (T), relative humidity (RH), boundary layer
height (BLH) and mass concentrations of $PM_{2.5}$ and the water-soluble ions in $PM_{2.5}$
during the observation period at the two sampling sites.

895

896

897

35

898
899
900
901
902

Figure 3 Diurnal variations in $PM_{2.5}$ and the boundary layer height (BLH) at the two
sampling sites.
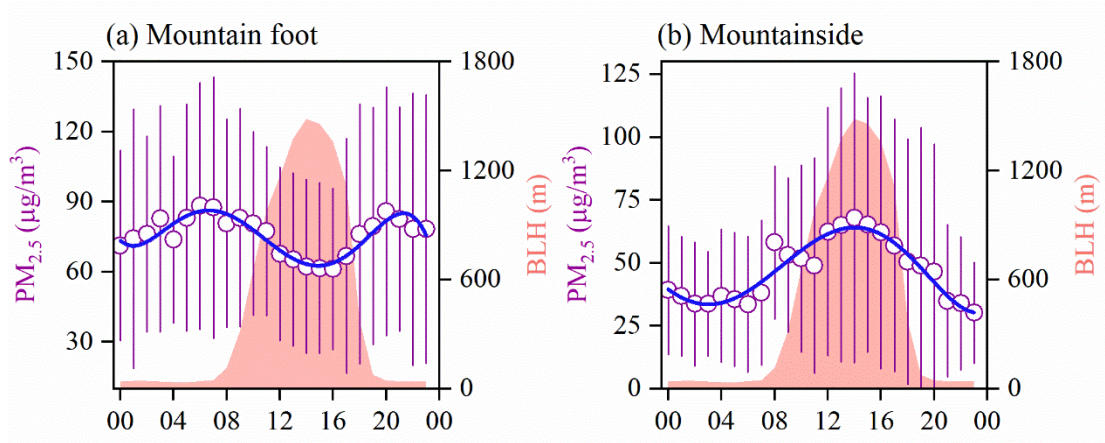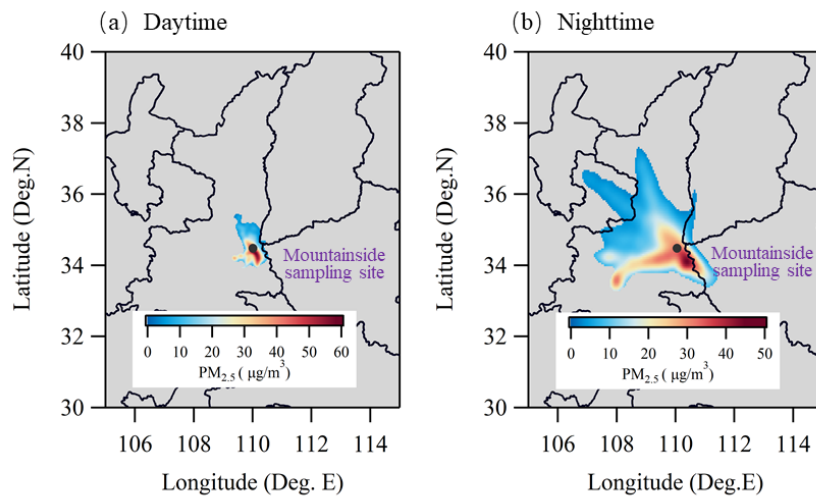
906
907
908
909
910
911
912

Figure 4 Concentration-weighted trajectory (CWT) analyses of $PM_{2.5}$ in both the
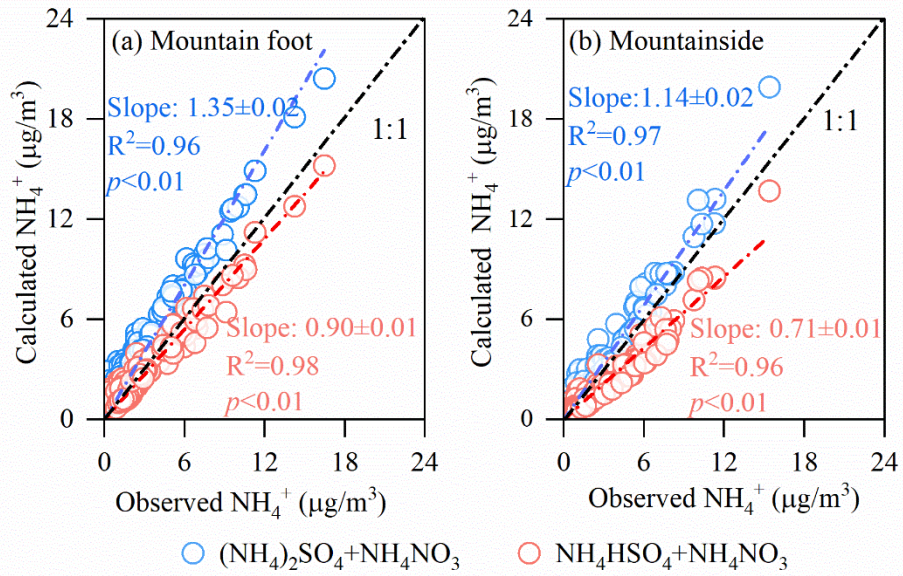daytime (8:00-20:00) and nighttime (21:00-7:00) at the MS site.
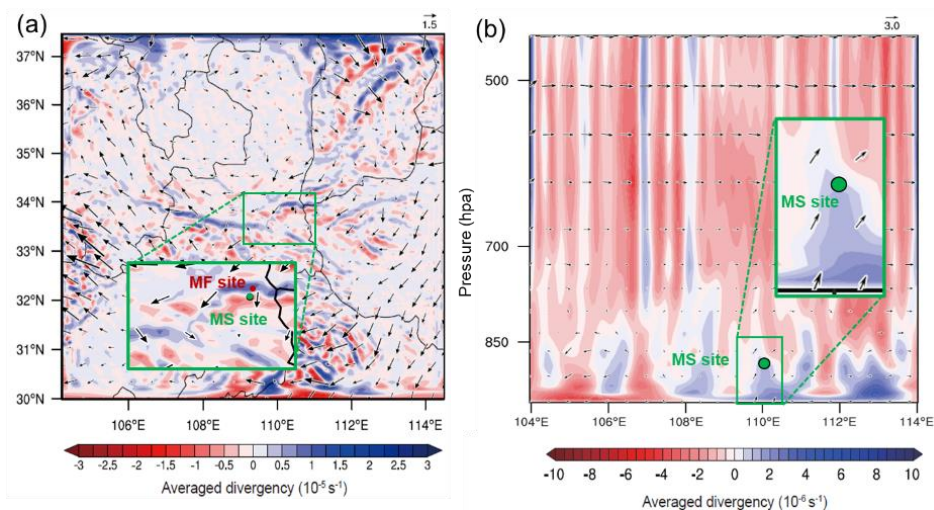
916
917
918

36

919
920
Figure 5 The distribution of averaged diurnal divergence over the whole campaign, with

corresponding wind filed. (a) Horizontal distribution at surface. (b) Longitude-pressure

cross-sections at 34°29′N. Wind speeds were represented by arrows sizes, and the W
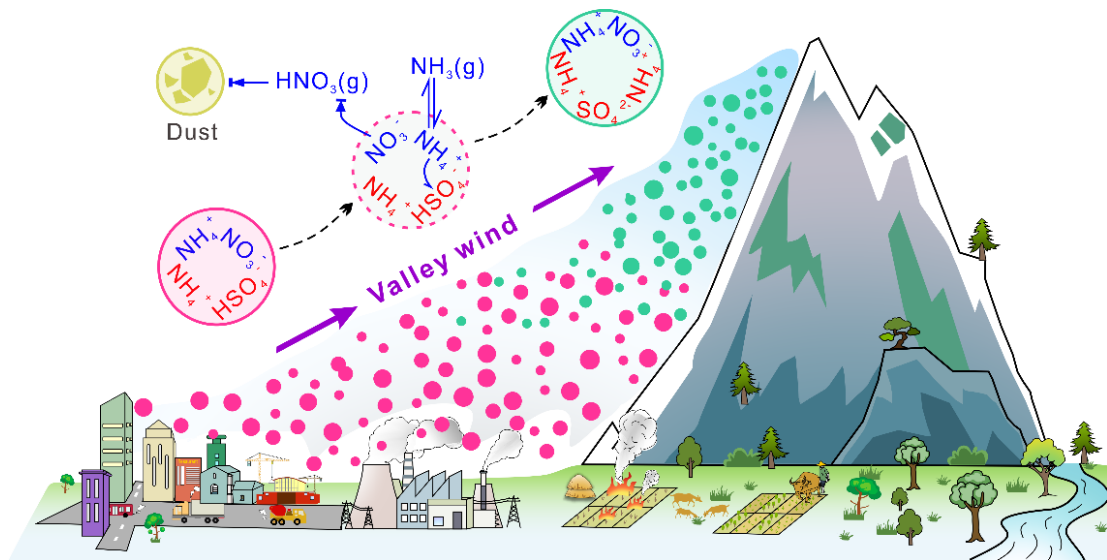
component of wind vectors was magnified 10 times.

925
926
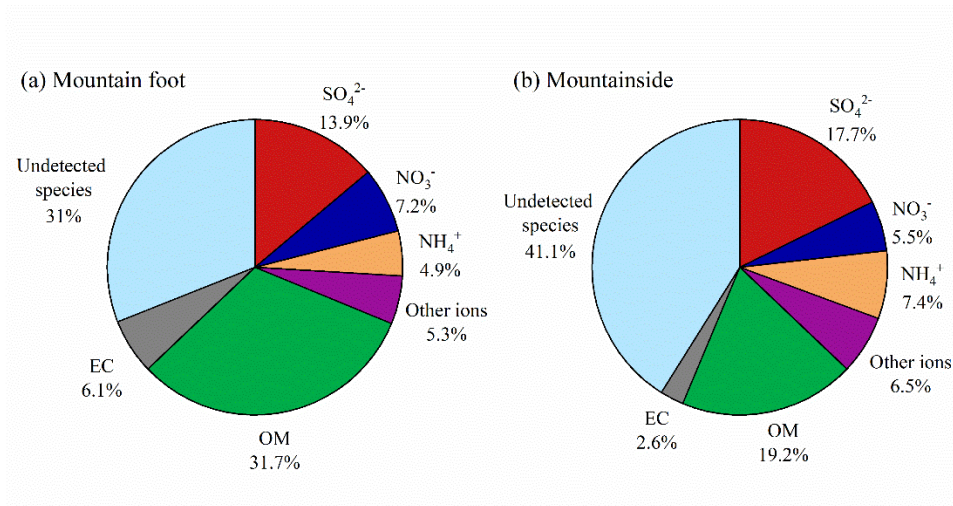
927
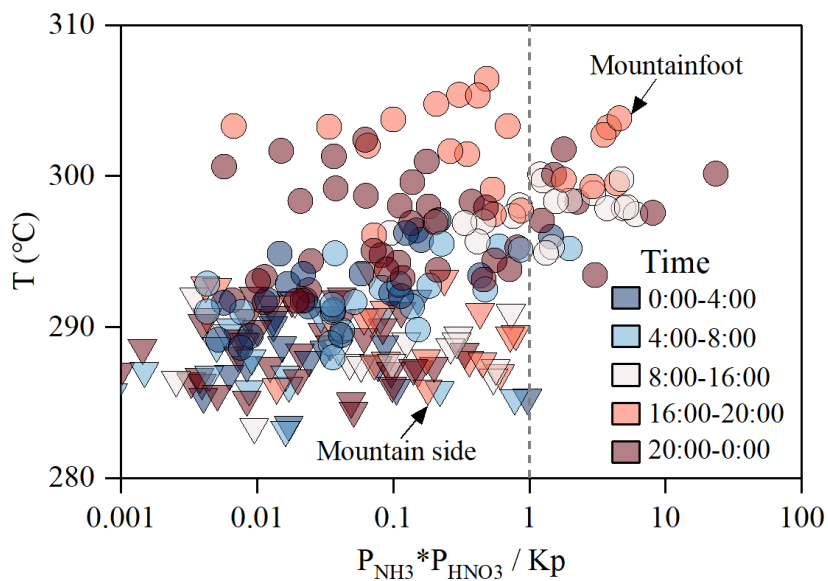Figure 6 Mass closure of $PM_{2.5}$ during the observed period (OM=1.6×OC).
929
930
931
932
933
934
935
936

937

Figure 7 Comparison of the calculated and observed NH_4^+ concentrations at both sampling sites.
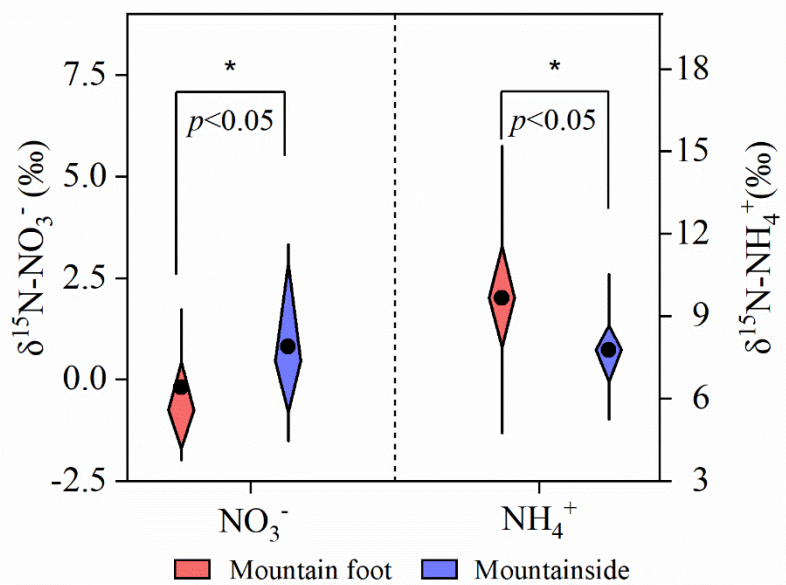
938
939
940
941
942
943
944

945

Figure 8 Schematic of the physicochemical behaviors of nitrate and ammonium during the transport process.

946
947
948
949

950
951 Figure 9 Temperature dependence of the ratio of the product of the partial pressures of
952 NH_3 and HNO_3 with the dry dissociation constant of NH_4NO_3.
953
954
955
956
957
958

959
960 Figure 10 Nitrate and ammonium $\delta^{15}N$ values at the two sampling sites in the daytime.
961